16.0 Stretching and Bending of Material Surfaces in Turbulence

First Prize - 1989 IBM 3090 Supercomputing Competition - Engineering

Stephen B. Pope[40], Pui-kuen Yeung[41] and Sharath S. Girimaji[42]

Sibley School of Mechanical & Aerospace Engineering
Cornell University
Ithaca, NY 14853

16.1 Abstract

In the study of mixing and reaction in turbulent flows, there are several phenomena that can be usefully described in terms of surfaces. Examples are turbulent flames and the turbulent mixing of different liquids. The most fundamental type of surface is the material surface which, by definition, moves with the fluid. Because of the fluid's turbulent motion and deformation, the surface is continually stretched and bent. In this study numerical simulations have been performed to understand and to quantify these processes.

A pseudo-spectral method is used to solve the Navier-Stokes equations which govern the motion of the fluid. These equations are solved on a 128^3 grid for the simplest possible turbulent flow — statistically stationary, homogeneous, isotropic turbulence. As the results show, the direct numerical representation of a material surface is not feasible: for the surface area grows exponentially (by a factor of10^{17} over the duration of the simulations); and radii of curvature less than a millionth of the grid spacing arise. Instead an indirect method is used in which ensembles (4-8,000) of infinitesimal surface elements are

---

[40] See "Stephen B. Pope" on page 969.

[41] See "Pui-Kuen Yeung" on page 975.

[42] See "Sharath S. Girimaji" on page 965.

followed. Statistics of interest are obtained from the stretching and curvatures of these elements.

For the first time, the mean rate of stretching has been determined. It is found that the surface area doubles every 2 1/2 Kolmogorov time scales. (The Kolmogorov time scale is the smallest physical time scale in turbulence.) While this is certainly rapid growth, it is only 40% of theoretical estimates, for reasons that are explained. Hitherto, little has been known about the curvature of material surfaces. The results show that extremely small radii of curvatures arise, as small as 10^{-8} of a Kolmogorov length scale (the smallest turbulent scale). These highly curved elements are found to be almost perfectly cylindrical in shape. Many other more refined statistics have been obtained.

The numerical simulations were performed on an IBM 3090-600E, with full exploitation of its vector, parallel and large-memory facilities. A typical run requires a total of 80 CPU hours, but can be completed in 20 hours because all six processors are used in parallel.

16.1.1 List of Index Terms

- Curvature of material surfaces
- Fluid mechanics
- Isotropic turbulence
- Kolmogorov scale
- Navier-Stokes
- Numerical simulations
- Pseudo-spectral method
- Surface stretching
- Turbulence
- Turbulent mixing

16.1.2 List of Contents

16.1.3 List of Figures

16.1.4 List of Tables

Stretching and Bending of Material Surfaces in Turbulence

16.2 Introduction

In the work described here, supercomputer calculations are used to answer fundamental questions of long standing about the effects of turbulence on material surfaces.

Turbulence — because of its importance in the atmosphere, the oceans, engineering equipment and elsewhere — has been the subject of theoretical study for over 75 years. In many areas, including the study of material surfaces, the theory is built on hypotheses that have not been tested because of insuperable experimental difficulties. Now, however, by simulating turbulence using a supercomputer it is possible to test these hypotheses. But much more: the simulations provide fresh insights into the basic physical processes of turbulence.

A material surface is defined by its initial condition (e.g. a specified plane at $t = 0$), and by the condition that every point on the surface moves with the local fluid velocity. We now provide two examples to illustrate the physical significance of these surfaces.

Figure 147 shows a sketch of the mixing of two bodies of water (A and B) in a closed vessel. Initially ($t = 0$) A contains a trace solute of concentration $\phi = \phi_0$, while B is pure water ($\phi = 0$). We consider the material surface that is initially coincident with the interface between A and B. The water is set in turbulent motion and as a result the material surface is convected, stretched and bent. In the first stages of mixing, the concentration is uniform everywhere except in the immediate vicinity of the material surface where there is a thin diffusive layer. Locally, the behavior of the diffusive layer is (to an excellent approximation) the same as a plane layer in a uniform strain field. Consequently, the mixing process can be completely analyzed in terms of the statistics of straining on the material surface [1, 2, 3]. (At later times the material surface folds over, and the analysis breaks down once the distance between folds is comparable to the diffusive-layer thickness.)

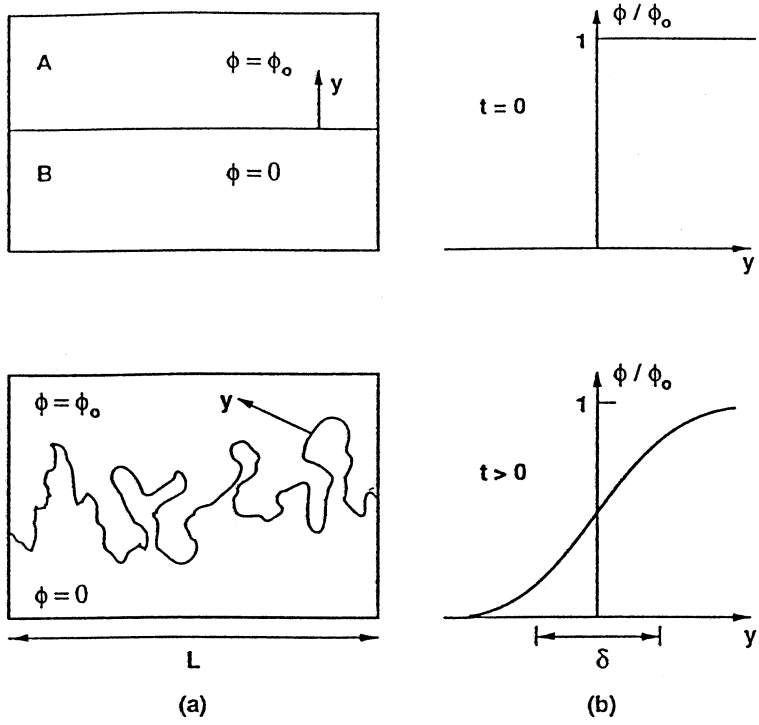

Figure 147. Mixing Between Two Bodies of Water. Sketch of the mixing between two bodies of water.
a) The material surface that initially (t = 0) separates A from B.
b)Normalized concentration profiles normal to the surface. (Note $\delta << L$.)

The second example is an idealization of a turbulent premixed flame (such as that in a spark-ignition automobile engine). Under appropriate conditions [4], there is a thin flame sheet that forms a connected but highly wrinkled surface that separates the reactants from the products (see Figure 148). This flame surface is convected, bent and strained by the turbulence, and propagates (relative to the fluid) at a speed w. If the propagation speed w is small compared to the turbulent velocity scales (in a way made precise in [3], then the flame surface behaves like a material surface. For this case the statistics of interest are, again, the straining on the material surface and also its curvature — for this affects the propagation speed w [5, 6].

The straining on material surfaces was first and most comprehensively studied by Batchelor [1, 7] over 30 years ago. He introduced two conjectures:

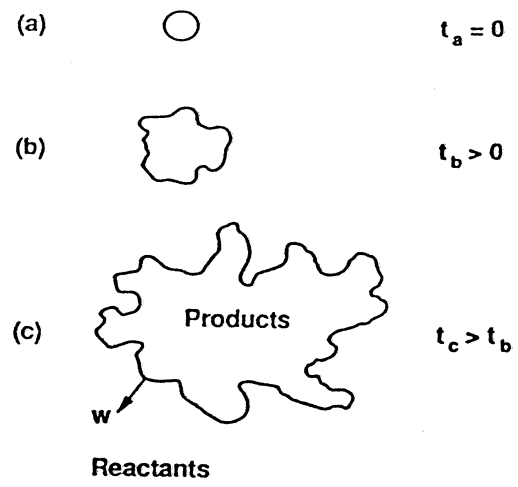

Figure 148. Development of a Turbulent Flame Sheet. Sketch of a turbulent flame sheet developing from an initially spherical kernel.

1. straining is persistent (i.e. the time scale of change of the strain rate is large compared to the time scale of strain itself);

and

2. the material surface becomes aligned with the principal axes corresponding to the two greatest principal strain rates.

Subsequent workers (see Monin and Yaglom [8] for a review) have accepted these conjectures and Corrsin [9] provides additional quantitative arguments for the persistence of strain.

The curvature of material surfaces has not been examined in as much detail, but it is often assumed (e.g. Klimov [10]) that

3. The radii of curvature of a material surface are no smaller than the smallest turbulence scales.

Because of insuperable experimental difficulties, these conjectures could not be tested experimentally. Our results show that none of them is correct.

The objective of the work described is to use simulations of turbulence to study the processes affecting material surfaces, in particular to characterize the statistics of surface straining and curvature.

The computational simulation of the turbulence is described in the next section, while the algorithm used to determine surface properties is described in 16.4, "Evolution of Material Surfaces." The results are given in 16.5, "Results and Discussion," and the paper closes with conclusions in 16.6, "Conclusions."

Space does not permit all the details to be presented here: more information can be found in previous works of the authors [2, 3, 11, 12, 13].

16.3 Turbulence Simulations

16.3.1 Pseudo-Spectral Method

The governing equations of fluid motion — the Navier-Stokes equations — are solved for the simplest possible turbulent flow: homogeneous, isotropic, statistically-stationary turbulence. Since, according to the Kolmogorov 1941 hypotheses [8], the small scales of turbulence are universal, the study of this simplest of turbulent flows has broad significance.

The Navier-Stokes equations are solved numerically using the pseudo-spectral method developed by Rogallo [14]. The time-dependent Eulerian velocity field, $\underline{u}(\underline{x}, t)$, is represented on an equispaced grid of N^3 grid points which form a cubic computational domain of length L_0. In the simulations reported N = 64 or N = 128. The velocity field is continued periodically (i.e., $\underline{u}(\underline{x} + \underline{z}L_0, t) = \underline{u}(\underline{x}, t)$, where $\underline{z}$ is any integer vector), and consequently $\underline{u}(\underline{x}, t)$ has a finite Fourier representation. There are N^3 corresponding discrete nodes in wavenumber space. Let $\underline{k}$ be the wavenumber vector at a given node, and k be its magnitude. The lowest nonzero wavenumber, denoted by k_0, is $2\pi/L_0$. The components of $\underline{k}$ are integer multiples of k_0, ranging from $(1\text{-}N/2)k_0$ to $(N/2)k_0$. We denote by $\hat{\underline{u}}(\underline{k}, t)$ the complex Fourier (wavenumber) coefficients of the velocity at time t: i.e., $\hat{\underline{u}}(\underline{k}, t)$ is the discrete Fourier transform of $\underline{u}(\underline{x}, t)$.

For each wavenumber, the Fourier velocity $\hat{\underline{u}}$ evolves by

$$\frac{d\hat{\underline{u}}}{dt} = \hat{\underline{a}}\,[\,\hat{\underline{u}}\,(t)\,]\,, \tag{1}$$

where $\hat{\underline{a}}$ (obtained from the Navier-Stokes equations) represents the velocity time derivative in wavenumber space and is dependent on $\hat{\underline{u}}$ at all $\underline{k}$. This (vector) equation is integrated in time by an explicit second-order Runga-Kutta method. The essence of the pseudo-spectral method is that the velocity products (that arise, for example, in the convective term) are evaluated in physical space, and then transformed to wavenumber space. This avoids the costly evaluation of the products in physical space as convolutions in wavenumber space. On the other hand, spatial derivatives (that would have to be approximated in physical space) are evaluated without approximation in wavenumber space. Most of the computational work (70% of it) is consumed in the Fast Fourier Transforms (FFT's) used to transform the data between physical and wavenumber spaces.

A forcing scheme [11] is used to maintain the turbulence energy against viscous decay. This is achieved by adding an artificial random term $\hat{\underline{a}}_F(\underline{k}, t)$ to the right-hand side of Eq. (1). It has been verified [15] that forcing the large-scale motions has a negligible effect on the small-scale motions that strain and bend material surfaces.

16.3.2 Implementation on the IBM 3090-600E

Rogallo's original pseudo-spectral code [14] was written in the Vectoral programming language and run on the Cray 1 computer at NASA Ames. Because of the very limited memory of this computer, a great deal of the coding is concerned with transferring data between memory and secondary storage.

While maintaining the same numerical algorithm, we completely rewrote the code in FORTRAN to exploit fully the vector, parallel and large-memory capabilities of the IBM 3090-600E. In a 128^3 simulation (i.e. N = 128) the grid consists of over 2 million nodes. As shown in Figure 149, these nodes can be considered to be N x-y planes (of N^2 nodes each), or as N x-z planes. The essence of the parallel implementation is to perform operations on planes of data, assigning each plane to a separate process. Thus in each phase of the calculations N processes are generated, each pertaining to an x-y or an x-z plane of data; and, at a given time, each of the 6 processors of the IBM 3090-600E is executing one of these processes. This is an extremely simple and effective use of parallelism which depends upon two properties: the large shared memory of the IBM 3090-600E; and, the ability to split the algorithm into operations requiring only

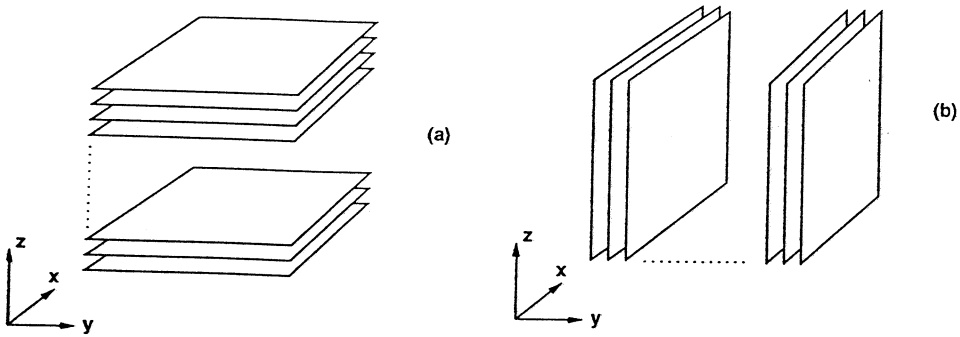

Figure 149. Data Structure. Sketch showing an N^3 of data as: a) N x-y planes, and b) N x-z planes.

lines or planes of data. The speed-up achieved (compared to using a single processor) is greater than 4.

The usual measures have been taken to exploit the speed-up made possible by the vector processors of the IBM 3090. Since about 70% of the CPU time is consumed in performing FFT's, particular attention was paid to their implementation. The ESSL vector routines are used for this purpose, with the optimum data structure and calling sequence having been determined by experimentation.

The computational requirements of a $(128)^3$ simulation are very large. Each time step takes a total of 2 CPU minutes, and a full run requires, typically, 2,400 time steps. Thus the total CPU time required is about 80 hours. However, because of the use of parallelism, the turnaround time can be less than 20 hours.

16.3.3 Physical and Numerical Parameters

Results are reported from four simulations, which are distinguished by the Reynolds number R_λ. Table 26 on page 495 contains a summary of the specified physical and numerical parameters and the resulting basic turbulence properties.

The accuracy of the simulations is determined by the spatial and temporal resolution. Detailed tests have been performed [11, 12, 15] to establish that resolution is excellent for all the simulations.

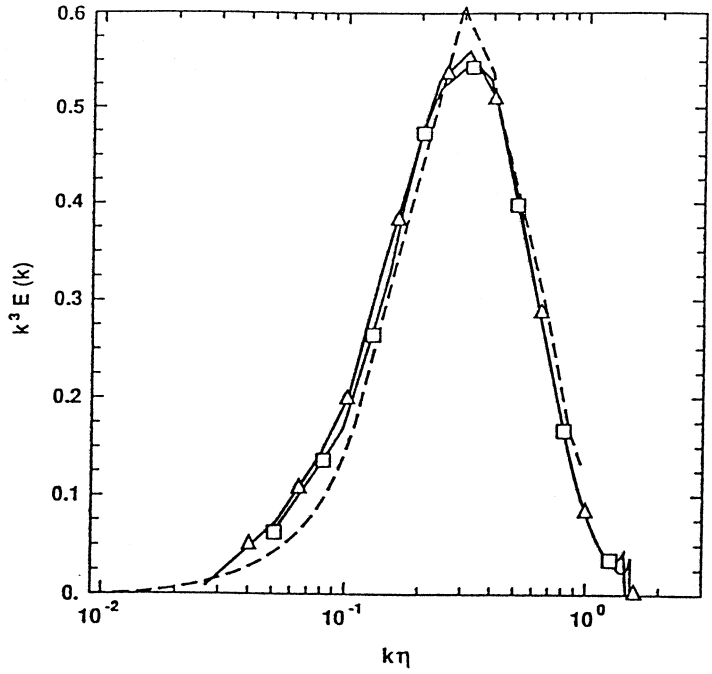

Figure 150. Spectrum Against Kolmogorov-Scaled Wavenumber. Spectrum $k^3E(k)$ (arbitrary scale) against Kolmogorov-scale wavenumber. △ $128^3 R_\lambda$ 63; □ $64^3 R_\lambda$ 59; dashed line, experimental data of Comte-Bellot & Corrsin [16], R_λ 65.

To illustrate the veracity of the simulations, on Figure 150 we show computed and experimentally measured dissipation spectra. With E(k) being the energy spectrum function, the quantity shown on the figure is proportional to $k^3E(k)$ — thus accentuating the high wavenumber (i.e. small scale) components of the velocity field. From this figure (and other tests performed [11, 12, 15]) we can conclude:

1. the spatial resolution is excellent (the whole dissipation spectrum is captured),
2. the small scale motions are unaffected by the details of the forcing,
3. the simulated small scales have the same statistics as experimentally realized turbulence.

16.4 Evolution of Material Surfaces

16.4.1 Direct Method

Given that the time-dependent three-dimensional velocity field $\underline{u}(\underline{x}, t)$ is known from the simulations described in the previous section, a direct method of the computing the evolution of a material surface immediately suggests itself.

For definiteness consider the material surface that initially ($t = 0$) is the plane $x_1 = 0$. Let $\underline{X}(t)$ denote the location of a point on the surface. Then, since by definition the surface moves with the fluid, we have:

$$\dot{\underline{X}}(t) \equiv \frac{d}{dt}\underline{X}(t) = \underline{u}(\underline{X}(t), t). \tag{2}$$

The direct method is to represent the surface discretely by M nodes, the m-th having position $\underline{X}^{(m)}(t)$. Because turbulence stretches and bends the surface, adaptive gridding (to re-position nodes and to introduce new ones) would be required to maintain resolution of the surface.

Our results show that the deformation of the surface is so severe as to make this approach impracticable. During the simulation the area of the surface increases by a factor of 10^{17}, and radii of curvature as small as 10^{-8} of a grid spacing occur. Clearly it is hopeless (and misguided) to attempt to represent such a massive surface with the necessarily fine resolution.

16.4.2 Infinitesimal Surface Elements

Rather than attempting to represent and resolve the whole surface, we study, instead, a large number (M = 4,096 or 8,192) of representative infinitesimal surface elements. A comprehensive account of the definition and properties of such elements is provided by Pope [2].

Figure 151 is a sketch of an infinitesimal surface element at time t. Its position is $\underline{X}(t)$, its infinitesimal area is $dA(t)$, and the unit normal to the surface is $\underline{N}(t)$. For each element, a time-dependent Cartesian coordinate system is introduced, with its origin at $\underline{X}(t)$, and with orthonormal basis vectors $\underline{e}_i(t)$ (i = 1,2,3). The unit vector $\underline{e}_3(t)$ is coincident with the normal, i.e. $\underline{e}_3(t) = \underline{N}(t)$, and consequently $\underline{e}_1(t)$ and $\underline{e}_2(t)$ are in the tangent plane of the surface at $\underline{X}(t)$. Initially at ($t = 0$) $\underline{e}_1(0)$ is specified arbitrarily in the tangent plane, and $\underline{e}_2(0)$ is determined by

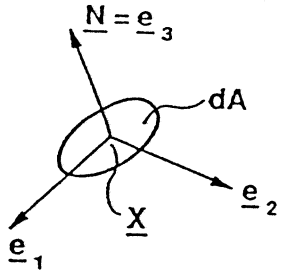

Figure 151. Sketch of an Infinitesimal Area Element

orthogonality. Subsequently, $\underline{e}_1(t)$ and $\underline{e}_2(t)$ rotate with the fluid. These specifications lead [2] to the following evolution equations:

$$\dot{\underline{e}}_\alpha = \frac{1}{2}\underline{e}_\beta\left\{\frac{\partial U_\beta}{\partial y_\alpha} - \frac{\partial U_\alpha}{\partial y_\beta}\right\}^0 + \underline{e}_3\left\{\frac{\partial U_3}{\partial y_\alpha}\right\}^0, \quad \dot{\underline{e}}_3 = -\underline{e}_\alpha\left\{\frac{\partial U_3}{\partial y_\alpha}\right\}^0 \tag{3}$$

Here y_1 and y_2 are coordinates in the $\underline{e}_1$ and $\underline{e}_2$ directions; Greek suffices take the values 1 or 2; the summation convention applies; $U_i \equiv \underline{e}_i \cdot \underline{u}$; and, the superscript 0 indicates that the quantities are evaluated at the origin.

With dA(t) being the infinitesimal area of the surface element, the area amplification factor A(t) is defined by A(t)≡dA(t)/dA(0). Note that A(0) is unity. The area increases due to straining according to

$$\dot{A} = Aa\,, \tag{4}$$

where $a(t) \equiv \left\{\frac{\partial U_\alpha}{\partial y_\alpha}\right\}^0$ is the rate of strain in the tangent plane.

The curvature of the infinitesimal surface element is completely described by the (second-order symmetric) curvature tensor $h^0_{\alpha\beta}(t)$ (see Pope [2]). The principal curvatures $k_1(t)$ and $k_2(t)$ are the eigenvalues of this tensor, with the convention $k_1 \geq k_2$. The exact evolution equation for $h^0_{\alpha\beta}$ is [2]:

$$\dot{h}^0_{\alpha\beta} = \left\{\frac{\partial^2 U_3}{\partial y_\alpha \partial y_\beta}\right\}^0 - a h^0_{\alpha\beta} - (s_{\gamma\beta}h^0_{\alpha\gamma} + s_{\gamma\alpha}h^0_{\beta\gamma}), \tag{5}$$

where $s_{\alpha\beta} \equiv \frac{1}{2}\left\{\frac{\partial U_\alpha}{\partial y_\beta} + \frac{\partial U_\beta}{\partial y_\alpha}\right\}^0$ is the strain-rate tensor in the tangent plane. (Note that $a = s_{\alpha\alpha}$.)

A complete set of equations has now been presented for the surface properties $\underline{X}$, $\underline{N} = \underline{e}_3$, $\underline{e}_\alpha$, A and $h^0_{\alpha\beta}$ (Eqs. 2-5). From given initial conditions, these can be integrated, given the time series of $\underline{u}$, $\partial u_i/\partial x_j$ and $\partial^2 u_i/\partial x_j \partial x_k$ following the fluid particle. Hence the curvatures k_1 and k_2 are determined as the eigenvalues of $h^0_{\alpha\beta}$.

Since the turbulence is isotropic, the initial condition $\underline{N}(0)$ is arbitrary. For convenience we specify $\underline{e}_i(0)$ to be coincident with the axes used in the Direct Numerical Simulation. The infinitesimal surface elements are specified to be plane initially: that is $h^0_{\alpha\beta}(0) = 0$.

16.4.3 Numerical Implementation

As the turbulence simulation steps through time, the set of ordinary differential equations describing the infinitesimal surface elements is solved by a second-order Runga-Kutta method for each of the M elements considered.

The set of differential equations for the elements (Eqs. 2-5) contains the velocity and its spatial gradients evaluated at the element location $\underline{X}(t)$. These quantities are obtained from the velocities at the grid nodes by cubic-spline interpolation, which has been shown to be extremely accurate [17]. The formation of the splines requires significant computational effort. It is implemented on the IBM3090 exploiting the parallel processing capabilities in much the same way as in the pseudo-spectral code.

16.4.4 Numerical Accuracy

The numerical accuracy depends on the spatial resolution (indicated by $\Delta x/\eta$ being small), and on the temporal resolution (indicated by $\Delta t/\tau_\eta$ and the Courant number C being small), where η and τ_η are the Kolmogorov length and time scales. For the Eulerian simulation it has been demonstrated in previous studies [11, 15, 17] that good resolution is achieved with $k_{max}\eta \approx 1.5$ (corresponding to $\Delta x/\eta \approx 2$) and $C \approx 0.5$

The results show that surface radii of curvature, R, less than a millionth of the Kolmogorov scale η are observed. Since both $\Delta x/R$ and the Courant number based on R can be very large ($\sim 10^5$), careful consideration needs to be given to whether numerical accuracy for the radii of curvature can, nevertheless, be claimed.

The sources of numerical error in determining $k_1(t)$ and $k_2(t)$ — beyond those incurred in the Eulerian simulation — are threefold. First there is the time-stepping error in integrating the surface-element ordinary differential equations. Inspection of Eq. (5) suggests that the time scale of change of k_α is no smaller than the Kolmogorov time scale τ_η: this is confirmed by the result. Hence the time step of size $0.1\,\tau_\eta$ is sufficiently small, as tests verify.

Second, there is some error involved in interpolating for the velocity derivatives. As the tests performed by Yeung and Pope [17] show, with the current resolution ($k_{max}\eta \approx 1.5$) and using cubic spline interpolation, this error is less than 1%.

Third, there is a numerical error (again investigated by Yeung and Pope [17]) in the integration of Eq. (2) to determine the element location $\underline{X}(t)$. Given the dispersive nature of turbulence, for t large compared to τ_η, this error could be large — certainly large compared to $10^{-6}\eta$. But the error in $\underline{X}(t)$ can, alternatively, be viewed as a small error in the initial condition. That is, the numerically determined particle position $\underline{X}(t)$ is the exact position of the particle originating from $\underline{X}(0) + \delta\underline{X}$ where $|\delta\underline{X}|$ is small (compared to η). And the time series of the velocity gradients of the particles originating from $\underline{X}(0)$ and $\underline{X}(0) + \delta\underline{X}$ differ little. Since we are interested in the statistics of a statistically homogeneous surface, the precise initial condition of the surface elements considered is unimportant.

In summary, in the current method of tracking infinitesimal surface elements, good resolution of the Kolmogorov length and time scales is sufficient for the accurate calculation of surface statistics. Resolution on the scales of the surface radii or curvature is not required. This conclusion is in marked contrast to that for the direct method (16.4.1, "Direct Method" on page 480) in which the whole surface is represented numerically.

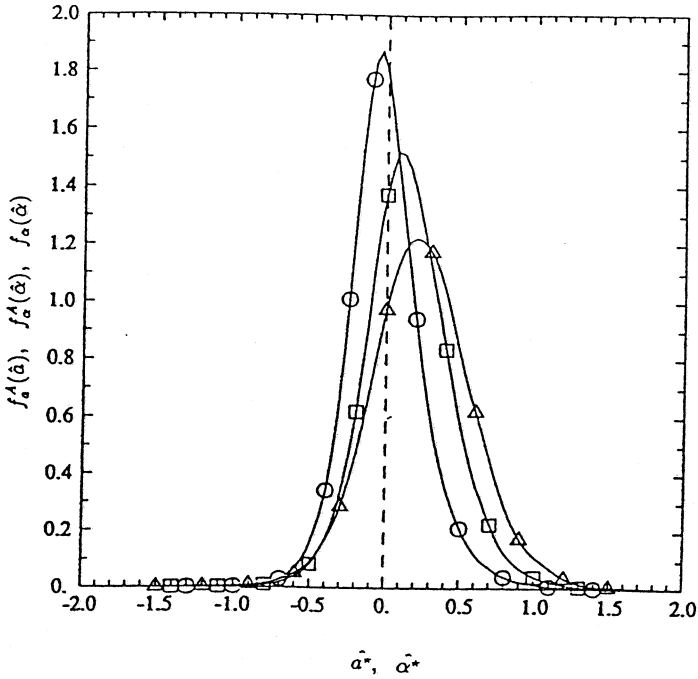

Figure 152. Probability Density Functions (pdf) of Surface Strain. Probability density functions of Kolmogorov-scaled strains acting on material and fixed surfaces. R_λ 93: △ a*(area-weighted); □ a*(unweighted); O α(for fixed surface).

16.5 Results and Discussion

16.5.1 Straining on Material Surfaces

In this subsection we first present statistics characterizing the straining of material surfaces. The fundamental quantity is a(t), the (total) rate of strain in the tangent plane of the material surface, which determines the rate of surface area increase (Eq. 4). It is appropriate to consider one-time area-weighted statistics, such that equal areas contribute equally to the mean. We note that straining statistics from our four simulations display no significant Reynolds number dependence [3].

The rate of strain in the tangent plane of a slowly propagating surface ($w \leq v_\eta$, where v_η is the Kolmogorov velocity scale) is well approximated by a; whereas for a rapidly propagating surface ($w \gg v_\eta$) it is close to α, the rate of strain acting on a randomly oriented element, which is statistically identical to $-\partial u_1/\partial x_1$. Figure 152 shows the area-weighted ($f_a^A(\hat{a})$) and unweighted ($f_a(\hat{a})$) probability density functions (pdf's) of a, and the pdf of $\alpha(f_\alpha(\hat{\alpha}) \approx f_\alpha^A(\hat{\alpha}))$. The strain rates are Kolmogorov-scaled ($a^\star = a\tau_\eta; \alpha^\star = \alpha\tau_\eta$).

It is seen that, relative to $f_a(\hat{a})$, $f_a^A(\hat{a})$ is displaced to the right, since large areas are associated with strong stretching (positive a). In fact, the area-weighted mean $< a^\star >_A = 0.28$ is almost twice the unweighted mean. The mean of α is identically zero, and its skewness is nearly 0.5, consistent with previous results [18]. The variance of $\alpha^\star$ is close to 1/15, its theoretical value in isotropic turbulence.

Two principal strain rates, S_1 and S_2 (with $S_1 \geq S_2$, and $S_1 + S_2 \equiv a$), are the eigenvalues of the strain-rate tensor in the tangent plane of a material surface $s_{\alpha\beta}$. The area-weighted joint pdf of Kolmogorov-scaled S_1 and S_2 ($S_1^\star = S_1\tau_\eta$, $S_2^\star = S_2\tau_\eta$) is shown in Figure 153. The isoprobability contours indicate that S_1 is almost always positive (with 98% probability), and that there is relatively high probability for the magnitude of S_2 to be small. The mean values of $S_1^\star$ and $S_2^\star$ are found to be approximately 0.315 and -0.035 respectively. The probability of net compressive straining in the tangent plane, i.e., $S_1 + S_2 < 0$, is about 19%.

We now examine the conjectures made by Batchelor [1, 7] on the straining of material surfaces (see 16.2, "Introduction"). As noted above, the area-weighted mean value of the surface strain is approximately $< a >_A = 0.28/\tau_\eta$. Thus the time scale of surface strain can be taken as $1/< a >_A \approx 3.5\tau_\eta$. The question of

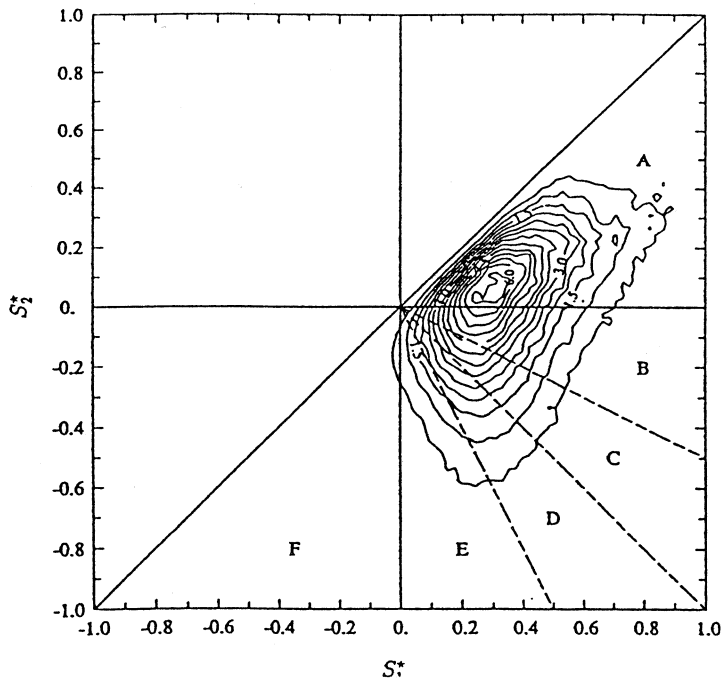

Figure 153. Joint pdf of Principal Surface Strains. Contour plot of the area-weighted joint pdf of the Kolmogorov-scaled principal surface strain rates S^*_1 and S^*_2. The indicated regions and their probabilities are:
A: $S_1 \geq S_2 \geq 0 \geq S_N$, Prob (A) = 0.498
B: $S_1 \geq 0 \geq S_2 \geq S_N$, Prob (B) = 0.201
C: $S_1 \geq 0 \geq S_N > S_2$, Prob (C) = 0.110
D: $S_1 \geq S_N \geq 0 \geq S_2$, Prob (D) = 0.100
E: $S_N > S_1 \geq 0 \geq S_2$, Prob (E) = 0.077
F: $S_N \geq 0 \geq S_1 \geq S_2$, Prob (F) = 0.014
where $S_N = -a = -S_1 - S_2$

whether the straining is persistent is best addressed by examining the two-time statistics of a, in particular its autocorrelation function. This is shown in Figure 154 for the R_λ 38 and R_λ 93 cases. It may be seen that the autocorrelation decays to small values well before a time lag of $3.5\tau_\eta$ is reached, and in fact crosses the zero line at about $2.75\tau_\eta$. The integral time scale of a is about $1.0\tau_\eta$ ($0.96\tau_\eta$ at R_λ 38, $1.03\tau_\eta$ at R_λ 93), which is small compared to $3.5\tau_\eta$. From these observations, we conclude that the time scale of change of strain is certainly not large compared to the time scale of strain itself — i.e., the straining on a material surface is not persistent.

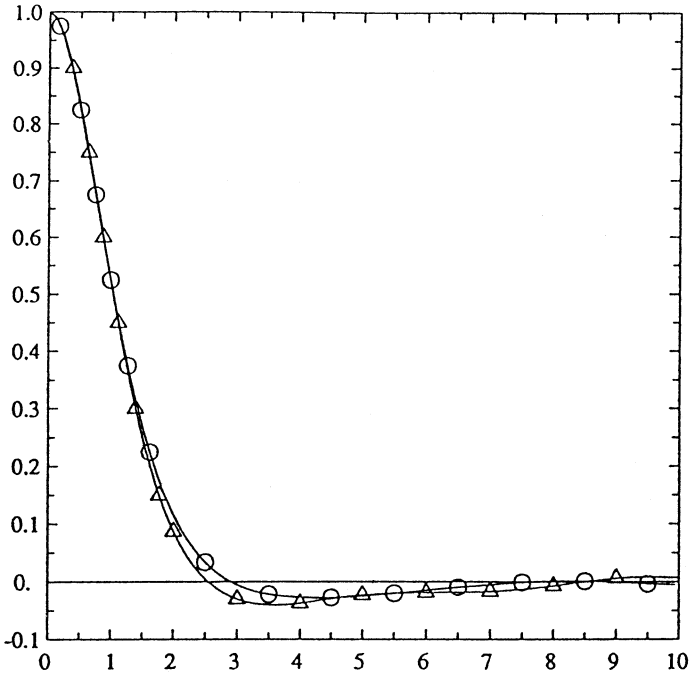

Figure 154. Autocorrelations of Surface Strain Rate a(t). Vertical axis is $\rho_a(\tau^*)$. Horizontal axis is $\tau^* \equiv \tau/\tau_\eta$. △ $R_\lambda = 38$ O $R_\lambda = 93$.

The second conjecture mentioned in 16.2, "Introduction" is that the surface element becomes aligned with the principal axes corresponding to the two greatest principal strain rates. Let Γ_A be the angle between the normal to the surface $\underline{N}$, and the principal axis corresponding to the least principal strain rate. Then the conjecture is equivalent to $\Gamma_A = 0$. Figure 155 shows the evolution of the mean $< \Gamma_A >$ from the simulations. Initially $< \Gamma_A >$ has a value close to unity, corresponding to the initial condition of Γ_A being uniformly random. After a transient, $< \Gamma_A >$ attains a value close to 0.75 radians. Clearly then, the conjecture ($\Gamma_A \approx 0$) is far from the truth.

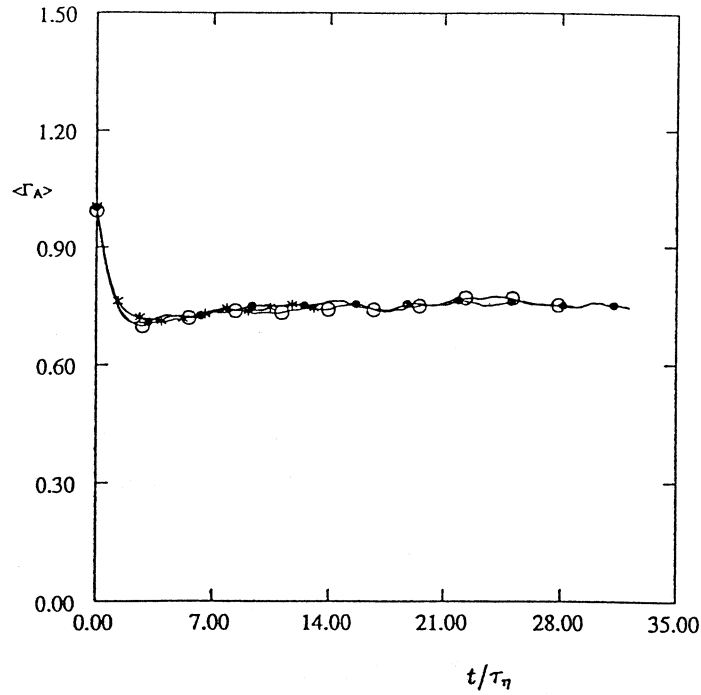

Figure 155. Evolution of The Mean Angle $<\Gamma_A>$. The evolution of the mean angle $<\Gamma_A>$ between the normal to the surface and the principal axis corresponding to the least principal strain rate: (O), R_λ 38; (•), R_λ 63; (★), R_λ 90.

16.5.2 Curvature of Material Surfaces

Curvature statistics have been determined for the R_λ 38 simulation, by calculating the properties of an ensemble of 8,192 infinitesimal surface elements. For each element the principal curvatures k_1 and k_2 are determined as the eigenvalues of $h^0_{\alpha\beta}$; and the area amplification A is used to construct area-weighted statistics [3].

The curvature is characterized by the following quantities: the normalized mean-square curvature, $M^\star(t)$, the logarithm of curvature, L, and , the normalized radius of curvature of the material element $R^\star(t)$:

$$L(t) \equiv \ln M^\star(t), \quad M^\star(t) = \frac{1}{2}\eta^2(k_1^2(t) + k_2^2(t)), \quad R^\star \equiv \frac{1}{\sqrt{2M^\star}} \tag{6}$$

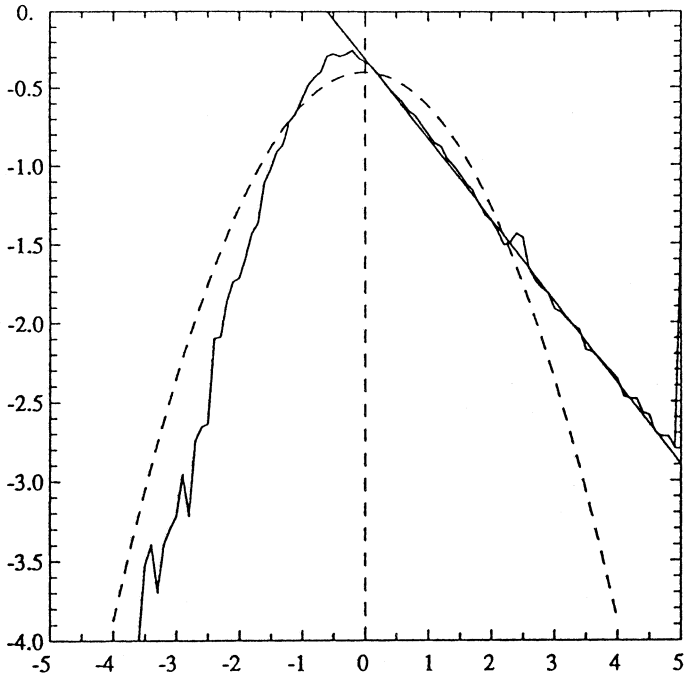

Figure 156. Standardized pdf of Logarithm of Curvature. Vertical axis is $\log_{10}[\hat{p}^A(\hat{l})]$. Horizontal axis is $\hat{l}$. Standardized area-weighted pdf of the logarithm of curvature L = lnM* (Eq. 12). Dashed line corresponds to lognormal distribution for M*; straight line corresponds to Eq. (16).

It is found that an essentially statistically stationary state is attained after about 15 Kolmogorov time scales. (Some subtleties about this state, and methods of reducing statistical errors in the state are discussed in Yeung et al.[3] and Pope et al.[12]). The area-weighted pdf $p^A(\hat{\iota})$ of the standardized logarithm of curvature, $\hat{L} = (L - < L >_A)/\sigma_A$, is shown in Figure 156. The mean and standard deviation of L are $< L >_A = -4.77$ and $\sigma_A = 2.18$. The dashed line on the figure is the parabola corresponding to the pdf if M* were log-normally distributed. Clearly the log-normal distribution does not, even qualitatively, describe the shape of the pdf.

It appears from the figure, that for large curvatures, the pdf of L, $p^A(\iota)$, has the asymptotic form

$$p^A(\iota) \sim b\, e^{-c\iota} \tag{7}$$

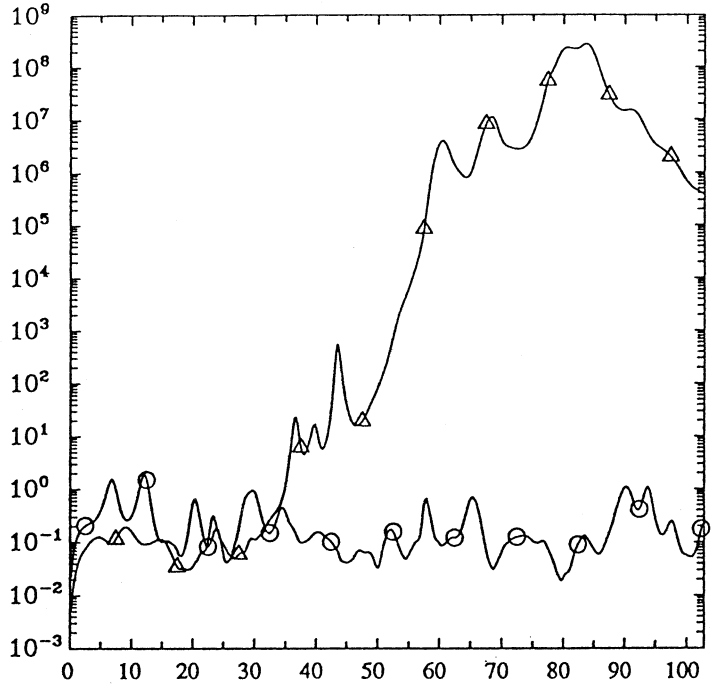

Figure 157. Time Series of Normalized rms Curvature. Verticle axis is $\sqrt{M^*(t)}$. Horizontal axis is t/τ_η. Normalized rms curvature against time for a typical element (O), and for the element that attains the greatest curvature (△).

with b = 0.0172 and c = 0.55. An immediate consequence of this result is that the expectation of the mean-square curvature $< M^\star >_A$ is infinite. For, if the integral converged, $< M^\star >_A$ would be given by

$$< M^\star >_A = \int_{-\infty}^{\infty} e^t p^A(t) dt. \tag{8}$$

Clearly, with the asymptotic form of Eq. (7) with c < 1, the integral does not converge.

To illustrate directly the occurrence of large curvatures, in Figure 157 we show the time series $\sqrt{M^\star}$ for the surface element that attains the largest value of M^* It can be seen that at parts it experiences a rapid rise in M^*, at the approximate exponential rate of $dL/dt \approx 1.8/\tau_\eta$. The peak value of $M^\star$ corresponds to a radius of curvature R less than $10^{-8}\eta$.

We examine in Figure 158 the area-weighted pdf $p_R^A(r)$ and the unweighted pdf $p_R(r)$ of the normalized mean radius of curvature (Eq. 6). The mean $< R^\star >_A$ is 12.0 (corresponding to about half the integral length scale). Even though the mean-square curvature $< M^\star >_A$ tends to infinity, Figure 158 shows that only about 5% of the surface has mean radius of curvature R smaller than the Kolmogorov length scale η. The unweighted and the area-weighted pdf's differ greatly, especially at the origin. The implication is that highly curved elements tend to have less area than more mildly curved elements.

The shape of the surface element at each point is determined by the relative values of the two principal curvatures. We define the shape parameter θ by $\theta = k_s/k_t$, where, k_s and k_t are the smaller and larger of k_1 and k_2 in absolute magnitude. Possible values of θ lie between -1 and $+1$. The value $\theta = 1$ corresponds to a spherical element; the value $\theta = 0$ corresponds to a cylindrical element; and the value $\theta = -1$ corresponds to a pseudo-spherical element.

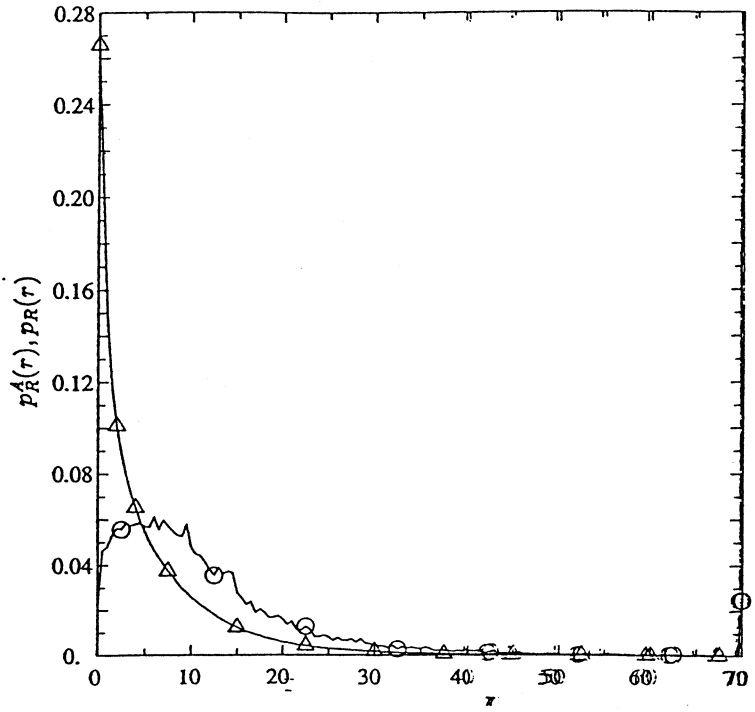

Figure 158. PDF of Normalized Mean Radius of Curvature. Area-weighted (O) and unweighted (△) pdf of normalized mean radius of curvature.

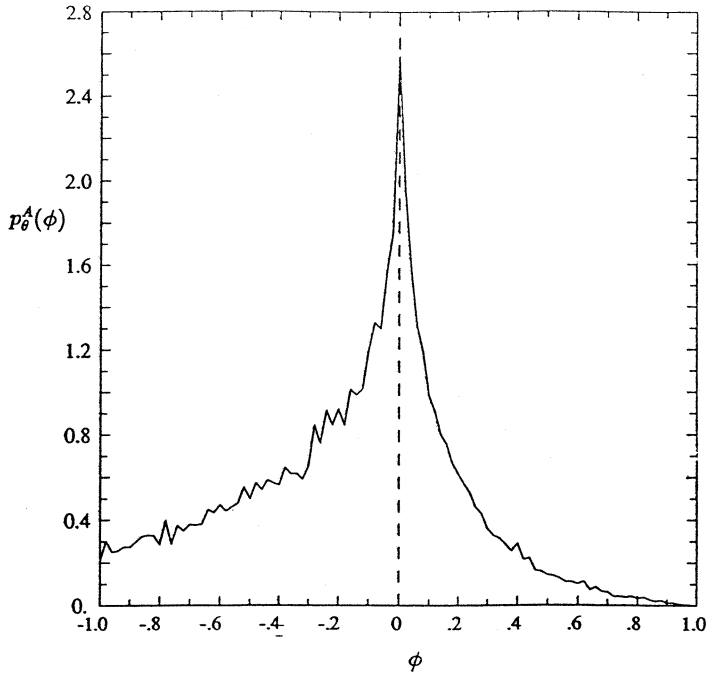

Figure 159. Area Pdf of the Shape Parameter θ. Area weighted pdf of the shape parameter Θ.

In Figure 159 we present the pdf of θ, and in Figure 160 a contour-plot of the joint pdf of θ and $\hat{L}$ is presented. From Figure 159 it is clear that the cylindrical shape is more probable, and the probability of a material element being spherical in shape is very small compared to either the cylindrical shape or the pseudo-spherical shape. The joint pdf of θ and $\hat{L}$ in Figure 160 shows that cylindrical shaped elements are associated with much higher than average curvatures, whereas the pseudo-spherical elements are more mildly curved.

16.6 Conclusions

Since the earliest work on turbulence almost a century ago, there has been no shortage of imaginative theories. But these theories have been based on hypotheses and conjectures that, at the time, were impossible to test. The present work clearly demonstrates that turbulence research is entering a new era, one in which supercomputers are used to extract detailed information about turbulence — information that can be used to test hypotheses and suggest new ones.

Contrary to previous wisdom, it has been shown that turbulent straining is fleeting, rather than persistent. As a consequence material elements do not become aligned with the principal axes of the strain time.

It is found that material surfaces become extremely contorted due to the straining and bending of the turbulence. Radii of curvature as small as 10^{-8} of

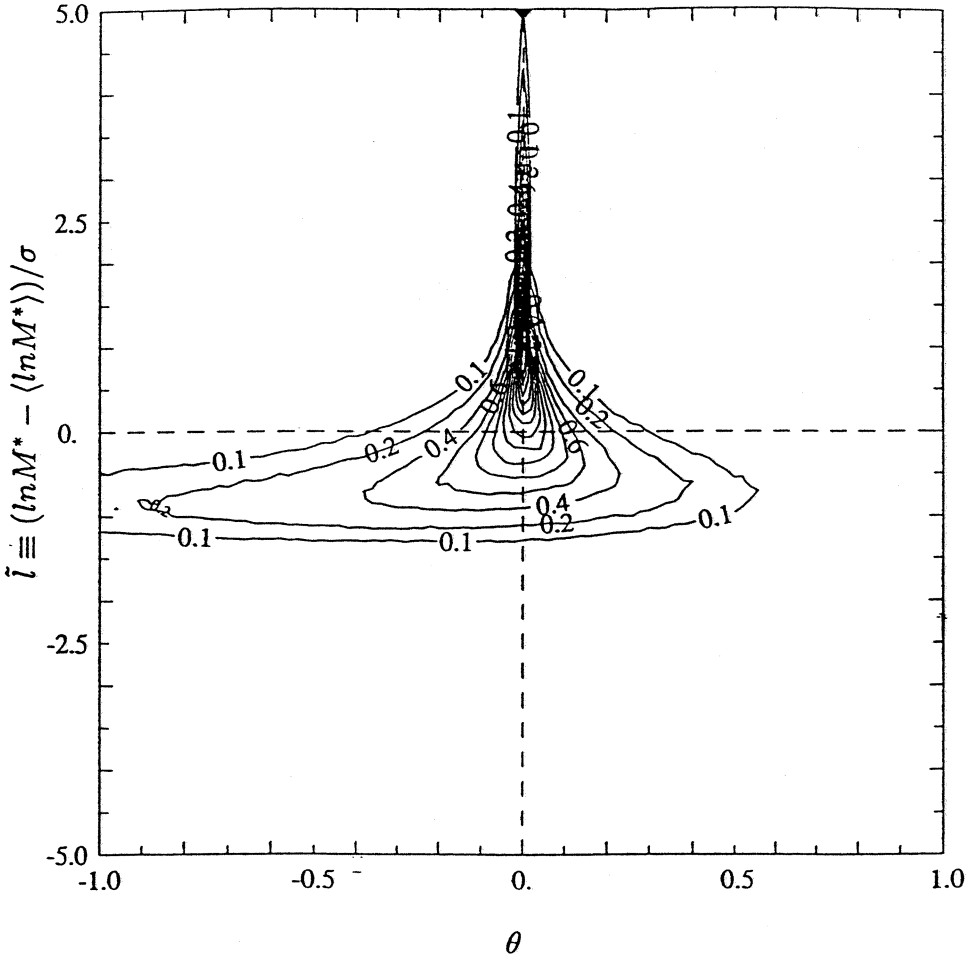

Figure 160. Joint pdf of ln M* and θ. Contour plot of the (unweighted) joint pdf of L = lnM* and Θ.

the Kolmogorov scale are observed. And these highly-curved elements are almost cylindrical in shape.

The simulations described here are for the simplest possible turbulent flow — homogeneous isotropic turbulence. But the result have general applicability since the behavior of the small scales is (nearly) universal — as evidenced by the lack of dependence of our results of Reynolds number R_λ.

16.7 Acknowledgements

This work was supported by the U.S. Air Force Office of Scientific Research (Grant No. AFOSR-88-0052). Computations conducted during the research were performed on the Cornell National Supercomputer Facility, which is supported in part by the National Science Foundation, New York State, the IBM Corporation and the members of the Corporate Research Institute.

Table 26. Numerical Parameters and Eulerian Statistics

Taylor-scale Reynolds number	R_λ	38	59	63	90	93
Grid Size	N	64	64	128	128	128
Length of solution domain	L_0	2π	2π	2π	2π	2π
Kinematic viscosity	ν	0.025	0.0158	0.0105	0.006546	0.006546
Turbulence intensity	u′	1.60	1.276	1.637	1.274	1.356
Dissipation rate	$<\varepsilon>$	2.69	0.775	2.673	0.780	0.893
Longitudinal integral length scale L_1	$\frac{L_1}{(\frac{1}{2}L_0)}$	0.369	0.528	0.321	0.448	0.398
Dissipation time scale $\tau_\varepsilon = \frac{3}{2}u'^2/<\varepsilon>$	τ_ε	1.43	3.184	1.510	3.174	3.099
Eddy turnover time $T_e = L_1/u'$	T_e/τ_ε	0.507	0.406	0.407	0.343	0.297
Kolmogorov time scale τ_η	$\tau_\eta/\tau_\varepsilon$	0.067	0.045	0.041	0.029	0.0028
Duration of simulation T	T/T_e	13.8	8.35	5.85	5.51	6.53
Time step Δt	$\Delta t/\tau_\eta$	0.52	0.042	0.024	0.027	0.029
Kolmogorov length scale η	η/L_1	0.042	0.029	0.025	0.018	0.019
Maximum resolved wavenumber k_{max}	$k_{max}\eta$	1.48	1.43	1.54	1.48	1.42
Taylor microscale λ	λ/L_1	0.521	0.437	0.399	0.326	0.359

16.8 References

1. G.K. Batchelor, *J. Fluid Mech.*, **5**, 113 (1959).
2. S.B. Pope, *Int. J. Engr'ng Sci.*, **26**, 445 (1988).
3. P.K. Yeung, S.S. Girimaji & S.B. Pope, *Combust. Flame*, **79**, 340 (1990).
4. S.B. Pope, *Ann. Rev. Fluid Mech*, **19**, 237 (1987).
5. B. Karlovitz, D.W. Denniston, Jr., D.M. Knappschaefer and F.E. Wells, *Fourth Symp. (Int'l) on Combust.*, p. 613, Williams & Wilkins (1953).
6. M. Matalon & B.J. Matkowsky, J. *Fluid Mech.*, **124**, 239 (1982).
7. G.K. Batchelor, *Proc. Roy. Soc.*, A, **213**, 349 (1952).
8. A.S. Monin & A.M. Yaglom, *Statistical Fluid Mechanics*, Vol. 2 (J.L. Lumley, Ed.) M.I.T. Press (1975).
9. S. Corrsin, J. *Atmos. Sci.*, **20**, 115 (1962).
10. A.M. Klimov, *Sov. Phys. Dokl.*, **20**, 168 (1975).
11. P.K. Yeung & S.B. Pope, *J. Fluid Mech.*, **207**, 531 (1989).
12. S.B. Pope, P.K. Yeung and S.S. Girimaji, *Phys. Fluids*, A, **1** 2010 (1989).
13. S.S. Girimaji & S.B. Pope, "Material Element Deformation in Isotropic Turbulence," *J. Fluid Mech.* (1990)(in press).
14. R.S. Rogallo, "Numerical Experiments in Homogeneous Turbulence," NASA TM 81315 (1981).
15. V. Eswaran & S.B. Pope, *Comput. Fluids*, **16**, 157 (1988).
16. G. Comte-Bellot and S. Corrsin, *J. Fluid Mech*, **48**, 273 (1971).
17. P.K. Yeung & S.B. Pope, *J. Comput. Phys.*, **79**, 373 (1988).
18. R.M. Kerr, *J. Fluid Mech*, **153**, 31 (1985).